Quadrupole collectivity in island-of-inversion nuclei ^{28,30}Ne and ^{34,36}Mg

S. Michimasa,[1,*] Y. Yanagisawa,[2] K. Inafuku,[3] N. Aoi,[4] Z. Elekes,[5] Zs. Fülöp,[5] Y. Ichikawa,[2] N. Iwasa,[3] K. Kurita,[6] M. Kurokawa,[6] T. Machida,[6] T. Motobayashi,[2] T. Nakamura,[7] T. Nakabayashi,[7] M. Notani,[8] H. J. Ong,[4] T. K. Onishi,[9] H. Otsu,[2] H. Sakurai,[9,2] M. Shinohara,[7] T. Sumikama,[3] S. Takeuchi,[2] K. Tanaka,[2] Y. Togano,[7] K. Yamada,[2] M. Yamaguchi,[2] and K. Yoneda[2]

[1]*Center for Nuclear Study, University of Tokyo, RIKEN Campus, 2-1 Hirosawa, Wako, Saitama 351-0198, Japan*
[2]*RIKEN Nishina Center, 2-1 Hirosawa, Wako, Saitama 351-0198, Japan*
[3]*Department of Physics, Tohoku University, Aoba, Sendai, Miyagi 980-8578, Japan*
[4]*Research Center for Nuclear Physics, Osaka University, Ibaraki, Osaka 567-0047, Japan*
[5]*Institute for Nuclear Research (ATOMKI), H-4001 Debrecen, POB.51, Hungary*
[6]*Department of Physics, Rikkyo University, 3-34-1 Nishi-Ikebukuro, Toshima, Tokyo 171-8501, Japan*
[7]*Department of Physics, Tokyo Institute of Technology, Meguro, Tokyo 152-8551, Japan*
[8]*Physics Division, Argonne National Laboratory, Argonne, Illinois 60439, USA*
[9]*Department of Physics, University of Tokyo, 7-3-1 Hongo, Bunkyo, Tokyo 113-0033, Japan*

(Received 15 October 2013; revised manuscript received 10 April 2014; published 7 May 2014)

The quadrupole collectivity of neutron-rich even-even neon and magnesium nuclei around $N = 20$, ^{28,30}Ne, and ^{32,34,36}Mg, was studied via proton inelastic scattering on a liquid hydrogen target by in-beam γ-ray spectroscopy in inverse kinematics. The angle-integrated cross sections for the first 2^+ states of these nuclei were determined by measuring de-excitation γ rays. The deformation lengths were extracted from the angle-integrated cross sections using distorted-wave calculations. The deformation length of ^{30}Ne ($\delta_{(p,p')} = 1.59^{+0.08}_{-0.09}$ fm) is smaller than that of ^{32}Mg ($1.83^{+0.10}_{-0.11}$ fm), which exhibits the largest quadrupole collectivity among the neutron-rich $N = 20$ isotones. Along the magnesium isotopic chain, the deformation lengths of ^{34}Mg and ^{36}Mg were deduced to be $2.30^{+0.09}_{-0.10}$ fm and $1.90^{+0.16}_{-0.17}$ fm, respectively. The evolution of quadrupole deformation in the vicinity of ^{32}Mg is discussed by comparing the present results with the theoretical calculations.

DOI: 10.1103/PhysRevC.89.054307 PACS number(s): 23.20.Lv, 25.60.−t, 25.40.Ep, 27.30.+t

I. INTRODUCTION

Recent experimental and theoretical studies on short-lived nuclei indicate that the shell structures of nuclei far from the valley of β stability cannot be interpreted using our knowledge established by studies for stable nuclei [1]. Indeed, disappearance of shell closures at the conventional magic numbers $N = 8$ [2–5], 20 [6–11], and 28 [12,13], and the development of magicity at $N = 16$ [14], 32 [15–17], and 34 [18], for example, in these respective neutron-rich regions are very intriguing phenomena. One of the most ambitious challenges in studies of unstable nuclei is to clarify the underlying nucleon-nucleon interactions by establishing the nuclear structure from stable nuclei to the drip line. To probe the driving forces behind these structural changes, it is necessary to measure systematically the physical quantities that characterize nuclear structure. Historically, the degree of collectivity is an important characteristic that can be investigated directly by deducing the quadrupole deformation length δ, or the deformation parameter β_2 ($= \delta/R$, where R is the nuclear radius). These quantities can be derived from the transition strength between the 0^+ ground state and first 2^+ state in even-even nuclei using various probes, for example, electromagnetic transition probabilities or proton inelastic scattering reactions [19,20].

In the present work, we have determined the quadrupole collectivity of neutron-rich nuclei around $N \sim 20$, the so-called island of inversion [9], using the proton inelastic scattering. The onset of significant deformation in this region was suggested for the first time owing to the large two-neutron separation energies of ^{31,32}Na [6]. Subsequently, the unexpected enhancement of collectivity in the region was confirmed experimentally from the low excitation energy of the first 2^+ state [8] and large transition probability, $B(E2)$, in ^{32}Mg [10]. It was suggested by several theoretical studies that the deformation in this region is caused by an enhancement of neutron np-nh excitations [7,9] that originate from a weakening of the *sd-pf* shell gap [11].

The experimental knowledge of the properties of nuclei on the neutron-rich side of the island of inversion was recently extended to include the excitation energies of the first 2^+ states in ^{32}Ne and ^{38}Mg, which are reported to lie at 722(9) keV [21] and 656(6) keV [22], respectively. In terms of the systematics of the energies of low-lying excited states around the island of inversion, the region of largest nuclear deformation corresponds to Ne and Mg isotopes at $N \geqq 20$. However, neither quadrupole deformation parameters nor deformation lengths have been reported for these nuclei; the present work addressed this fact and the evaluation of quadrupole collectivity of neutron-rich nuclei in this region will be discussed in light of the new results.

In studies of quadrupole collectivity involving the proton inelastic scattering, ambiguity generally prevails in a choice of optical potential. In the present study, we adopted

*mitimasa@cns.s.u-tokyo.ac.jp

optical-potential dependence by using the recently published optical potential for light unstable nuclei [23] and compared the results to older optical potentials [24,25] adopted in previous studies.

However, despite this disadvantage, the proton inelastic scattering in a liquid-hydrogen target has one noble advantage, namely, the number of statistics that can be achieved in an experiment. The technique provides a high luminosity because of the number of target atoms [26]: The density of liquid hydrogen is typically 100 times larger than high-Z targets that are adopted for Coulomb excitation studies. Accordingly, we successfully measured the quadrupole collectivity of very neutron-rich nuclei supplied as radioactive-ion (RI) beams with relatively low intensity [26–29]. In the present work, we report here the experimental results on ^{28,30}Ne and ^{32,34,36}Mg.

II. EXPERIMENT

The experiment was performed at the RI Beam Factory, operated by RIKEN Nishina Center and Center for Nuclear Study, the University of Tokyo. A ^{48}Ca primary beam was accelerated up to 63 MeV/nucleon by the acceleration scheme of RFQ-RILAC-CSM-RRC [30]. The radioactive secondary beam, containing neutron-rich nuclei ^{32,34,36}Mg and ^{28,30}Ne, was produced by fragmentation reactions with ^{181}Ta and enriched ^{64}Ni foils with respective thicknesses of 150 and 200 μm. The beam constituents were identified using the RIKEN projectile-fragment separator (RIPS) [31]. The magnetic field of RIPS was set to optimize the yield of the $A/Z = 3$ products, namely, ^{30}Ne and ^{36}Mg. An 81-μm-thick wedge-shaped degrader was installed at the first dispersive focal plane. Particle identification was made on an event-by-event basis by measuring the magnetic rigidity ($B\rho$), time of flight (TOF), and energy loss (ΔE); Fig. 1(a) indicates the constituents of the secondary beam. The average energy at the center of the reaction target and the total momentum acceptance of ^{36}Mg were 44.5 MeV/nucleon and 6%, respectively. Accordingly, a total intensity of 0.3 particles per second of ^{36}Mg was achieved. Specific details of the beam fragments are summarized in Table I. A schematic view of the experimental setup around the secondary target is provided in Fig. 2. The secondary target was

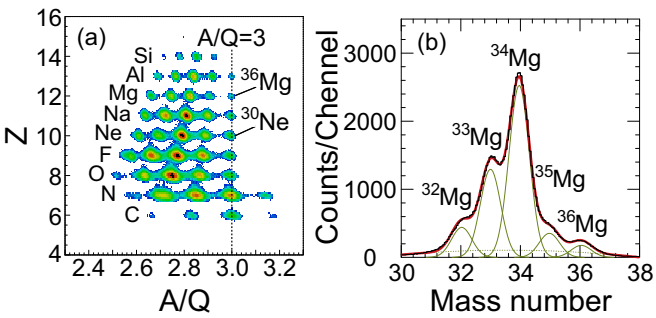

FIG. 1. (Color online) Particle identification of (a) the incident particles and (b) outgoing magnesium isotopes. The horizontal and vertical axes of the panel (a) show the A/Q and Z of the particles, respectively. Panel (b) shows the mass spectrum of outgoing magnesium isotopes.

TABLE I. The mean energies at the center of the secondary target and the total numbers of incident ^{28,30}Ne, ^{32,34,36}Mg particles.

Nucleus	Mean energy (MeV/nucleon)	Total number (particles)
^{28}Ne	53.5	1.26×10^6
^{30}Ne	44.0	1.65×10^5
^{32}Mg	58.9	5.03×10^4
^{34}Mg	51.1	3.53×10^5
^{36}Mg	44.5	3.40×10^4

a 95-mg/cm^2-thick liquid hydrogen vessel that was produced and maintained by the CRYPTA system [32]. The entrance and exit windows of the target consisted of 6-μm Havar foils. The contribution of the target windows to the proton inelastic cross sections is estimated to be less than 1% because the number of atom in the foils was 550 times smaller than the number of the hydrogen atom in the target.

The scattered particles were analyzed by the TOMBEE spectrometer [34], which consists of a superconducting triplet quadrupole (STQ) [35], plastic scintillators for measuring time of flight, and a ΔE-E telescope. The plastic scintillators were installed 3.8 m apart: The first was located 50 cm downstream from the liquid hydrogen target and the second was placed at the final focus of the spectrometer. The ΔE-E telescope, which consisted of a silicon detector and a NaI(Tl) detector was also mounted at the final focus. The silicon detector has a 134-mm diameter and a thickness of 320 μm. The NaI(Tl) detector has an effective area of 120 $\times$ 120 mm^2 and a thickness of 60 mm, and was constructed from two separate scintillator crystals each with photomultiplier tubes. The atomic (Z) and mass (A) numbers of each particle were determined by using the TOF-ΔE and TOF-E methods, respectively. The resolutions in Z and A for magnesium isotopes were estimated to be 1.8% and 2.3% (FWHM), respectively, which corresponds to a 3σ separation of the isotopes; the mass distribution of magnesium isotopes is provided in Fig. 1(b). The transmission efficiency of TOMBEE was estimated to be 96% and 50% at $\theta_{\rm lab} = 0^\circ$ and 2.6°, respectively, from scattered magnesium isotopes.

The energies of nuclear excited states populated by inelastic scattering were deduced from γ rays measured in coincident with incident and scattered nuclei. The γ rays were detected by the DALI2 array [33], which consisted of 160 NaI(Tl) crystals that surrounded the reaction target. The energy calibration and detection efficiency of DALI2 were deduced

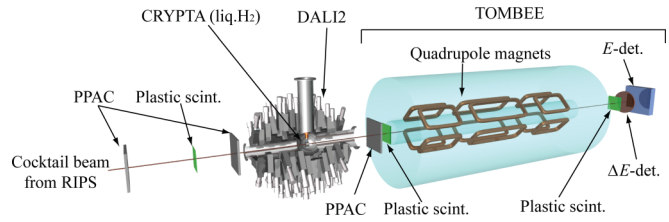

FIG. 2. (Color online) Arrangement of the beam-line detectors, CRYPTA [32], DALI2 [33], and TOMBEE [34] in the present experiment.

using standard ^{137}Cs, ^{60}Co, and ^{88}Y sources. The uncertainty in the energy calibration was estimated to be <0.5%, and the detection efficiency at 662 keV (from ^{137}Cs) was estimated to be 23.9%.

During the experiment, the de-excitation γ rays were emitted from nuclei moving at ∼30% of the speed of light. To correct the Doppler shift effect, the emission angles of the γ rays were determined from the trajectories of the scattered particles and the positions of the NaI(Tl) crystals. To measure the scattering angles, two parallel-plate avalanche counters (PPACs) [36] were installed upstream from the reaction target, and one PPAC was installed downstream (see Fig. 2). The two upstream PPACs were used to determine the incident angle and hit position on the target, while the downstream PPAC was used to deduce the scattering angle by combining the information on the hit position.

To extract the γ-ray relative intensities from experimental energy spectra, Monte Carlo simulations with the GEANT libraries [37] were employed. The simulation took into account the geometries of DALI2, CRYPTA, and beam pipes as well as the spatial, angular, and velocity spreads of the radioactive beam. The detection efficiency of DALI2, obtained using stationary γ sources, was reproduced within 3%.

III. RESULTS

A. Cross sections to the 2_1^+ states

The angle-integrated cross sections for population of the 2_1^+ states were calculated from the yields of the $2_1^+ \rightarrow 0_1^+$ transition with the requirement of γ-ray multiplicity (M_γ) equal to one (M_γ is defined as the total number of γ rays detected in coincidence with a single particle event). As demonstrated in Ref. [28], selection of $M_\gamma = 1$ efficiently eliminates the γ rays that depopulate higher-lying states in a cascade owing to the high total detection efficiency of the DALI2 (∼80%). Note that the GEANT simulations also reproduced the total efficiency and response function for γ cascade events in a satisfactory manner and, therefore, selection of $M_\gamma = 1$ events provides an efficient tool to determine population cross sections for the 2_1^+ state, even in cases where γ-γ analysis is difficult because of low beam intensities. We will demonstrate the validity of the M_γ selection method for deducing the cross sections for the 2_1^+ states in the present data for ^{28}Ne and ^{32}Mg nuclei, because the excited states and deformation lengths of these nuclei have been reported in previous studies [29,38].

1. ^{28}Ne

As indicated in Table I, the number of statistics for ^{28}Ne in the present data was significantly larger than for $A/Z = 3$ nuclei and, therefore, we were able to determine the cross section for the population of the 2_1^+ state using both the M_γ selection method and a γ-γ coincidence analysis. The γ-ray energy spectra for ^{28}Ne with $M_\gamma = 1$ and $M_\gamma \geqq 1$ conditions are displayed in Figs. 3(a) and 3(b), respectively. The background spectrum (thin green histogram) was obtained using a time window that was shifted relative to the prompt time window. Note that the background spectrum was normalized

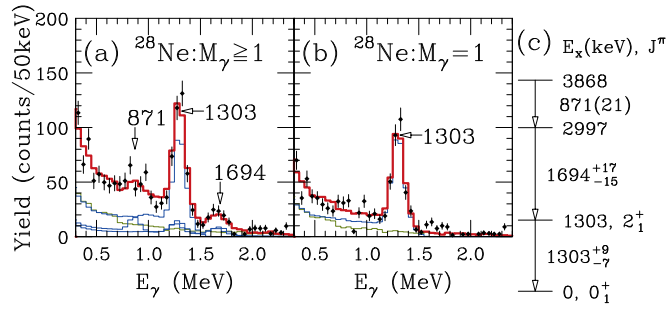

FIG. 3. (Color online) Gamma-ray energy spectra for the ^{1}H(^{28}Ne,^{28}Neγ) reaction. Panels (a) and (b) were obtained with no multiplicity cut and a $M_\gamma = 1$ condition, respectively. The solid circles with error bars indicate the experimental data. The thin green and blue histograms are the background and simulated spectra, respectively. The thick red histogram is the sum of the green and blue lines. Panel (c) displays the γ transitions in ^{28}Ne, which were measured by the present work.

using the relative widths of the background and prompt time windows.

In the present work, the $2_1^+ \rightarrow 0_1^+$ transition for ^{28}Ne is reported at 1303^{+9}_{-7} keV. In panel (a), the two additional peaks lie at 871(21) and 1694^{+17}_{-15} keV. Using γ-γ coincidences, we conclude that the 871-, 1694- and 1303-keV lines form a γ-ray cascade, as displayed in Fig. 3(c). This is consistent with the 1304(3)-1706(5)-894(3) decay sequence reported in Refs. [39,40].

The cross sections for population of the 1303-, 2997- and 3868-keV states were obtained by a decomposition analysis of the observed γ-ray spectrum using simulated response functions of the γ rays that depopulate these three states [29,41]. The strength of each response function corresponds to the cross section for the corresponding state. The cross sections deduced from the decomposition analysis and the γ-γ coincidence analysis were consistent. The respective cross sections to these states were determined to be 23(2) mb, 4(1) mb, and 3(1) mb in the present work. Using the $M_\gamma = 1$ spectrum of Fig. 3(b), the yield of the 1303-keV line was analyzed with the simulated response functions. The cross section that extracted when using only a simulated response function for the 1303-keV transition is 24(2) mb, which agrees well with the value quoted above.

Therefore, the cross section obtained from the $M_\gamma = 1$ data is reliable for determining the cross section for the 2_1^+ state of ^{28}Ne. When the 1303-, 2997- and 3868-keV transitions were included in the estimation, the obtained cross section is identical with the decomposition analysis. The cross section for the 2_1^+ state is given as 23(2) mb for the reminder of the discussion of the present work. It is worthwhile noting that this value is consistent with the previous measurement [22(5) mb] reported by Dombrádi *et al.* [38].

2. ^{32}Mg

Using the ^{32}Mg data, we demonstrate the effectiveness of M_γ selection in determining the cross section for the 2_1^+ state for cases with low statistics. In the present experiment, the

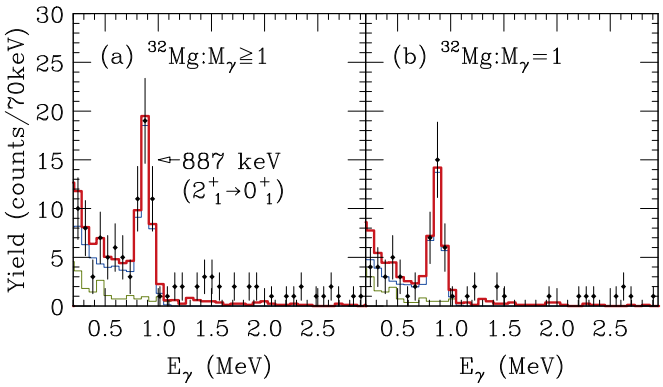

FIG. 4. (Color online) Same as Fig. 3, but for the ^{1}H(^{32}Mg,^{32}Mgγ) reaction.

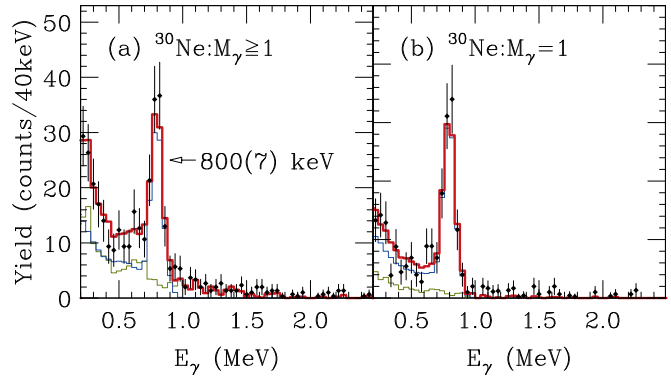

FIG. 5. (Color online) Same as Fig. 3, but for the ^{1}H(^{30}Ne,^{30}Neγ) reaction.

intensity of ^{32}Mg was significantly lower than that of ^{28}Ne and similar to that of ^{36}Mg, owing to the fact that only the edge of the ^{32}Mg momentum distribution was accepted by the spectrometer.

The $M_\gamma \geqq 1$ and $M_\gamma = 1$ spectra for ^{32}Mg are provided in Figs. 4(a) and 4(b), respectively. The cross section for population of the 2^+_1 state was extracted to be 40^{+9}_{-8} mb from the $M_\gamma = 1$ data, while the cross section for the $2^+_1 \rightarrow 0^+_1$ transition, which contains feeding from the higher lying states, amounted to be 56^{+9}_{-8} mb. These are consistent with a previous report, 47.6(53) mb and 63.2(54) mb, respectively [29], where the same reaction at a similar energy (46.5 MeV/nucleon) was studied with higher statistics and a detailed γ-γ analysis was performed. Importantly, the results highlight the validity of the analysis technique for cases with both high- and low-statistics data.

3. ^{30}Ne

The γ-ray energy spectra measured in coincidence with inelastically scattered ^{30}Ne are shown in Figs. 5(a) and 5(b), for $M_\gamma \geqq 1$ and $M_\gamma = 1$, respectively. The strongest peak, that at 800(7) keV, corresponds the $2^+_1 \rightarrow 0^+_1$ transition, and is consistent in energy with the previous works [21,26,42]. In Ref. [42], a cascade involving transitions at 792 and 1443 keV transitions from the 2235-keV state was reported. However, this cascade could not confirm by the present work. The cross section for the 2^+_1 state was deduced to be 37(4) mb using the spectrum in Fig. 5(b). The strength of the $2^+_1 \rightarrow 0^+_1$ transition, extracted from Fig. 5(a), which may contain contributions from the higher-lying states, is 39(5) mb. However, these two values are consistent within uncertainties and, therefore, contributions from higher-lying states are not significant. Moreover, the present result is consistent with the reported total strength of 30(18) mb [26].

4. ^{34}Mg

The γ-ray spectra of inelastic scattering of ^{34}Mg are shown in Fig. 6; panels (a) and (b) provide the singles γ spectrum ($M_\gamma \geqq 1$) and $M_\gamma = 1$ spectrum, respectively. In both panels, a prominent peak lies at 658(4) keV, which is assigned as the $2^+_1 \rightarrow 0^+_1$ transition. The first 2^+ state in ^{34}Mg was previously reported at 660 keV [43–46], and is, therefore, consistent with the present result.

In Fig. 6(a), weaker transitions around 1.4 and 2.5 MeV were also observed. γ-γ coincidences were examined to confirm whether these γ rays form cascades with the $2^+_1 \rightarrow 0^+_1$ transition. Figure 7 shows γ-ray energy spectra measured in coincidence with the 660-keV line; Fig. 7(a) provides the spectrum from the fragmentation of nuclei heavier than ^{34}Mg in the secondary beam while Fig. 7(b) indicates the spectrum deduced from the inelastic scattering reaction. In both channels, the two peaks at around 1.4 and 2.5 MeV could be identified. Accordingly, it is concluded that these lines correspond to the two weaker γ-ray peaks in Fig. 6(a) that were discussed above. The energies of these transitions were deduced to be 1353^{+29}_{-27} keV and 2536^{+34}_{-33} keV, respectively, indicating additional excited states in ^{34}Mg at 2011 and 3194 keV, which are shown in the level scheme of Fig. 7(c). With the exception of the $2^+_1 \rightarrow 0^+_1$ transition, the previous studies reported γ-ray lines in ^{34}Mg at 1460(20) keV [43], and 1395(15), 2480(30), and 3130(30) keV [22]. Note that the 1353- and 2536-keV transitions identified in the present work are consistent in energy with 1395- and 2480-keV transitions reported in Ref. [22] owing to the relatively large uncertainties.

From the analyses of the γ-ray yields of the peaks in Fig. 6(a) and in the γ-γ coincidence spectrum of Fig. 7(b),

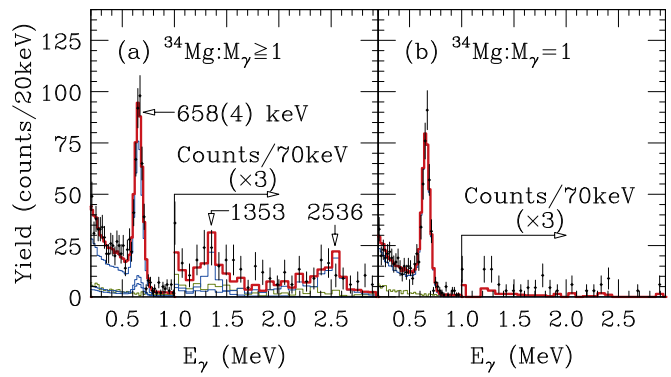

FIG. 6. (Color online) Same as Fig. 3, but for the ^{1}H(^{34}Mg,^{34}Mgγ) reaction.

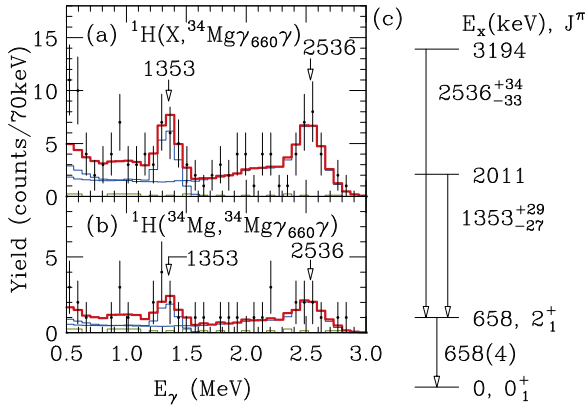

FIG. 7. (Color online) Gamma-ray energy spectra measured in coincidence with the 660-keV line in ^{34}Mg. Panel (a) was obtained with no selection of incident particles. Panel (b) shows the result for the inelastic reaction channel. The solid circles with error bars represent the experimental data. The thin green and blue histograms show the background and simulated γ spectra, respectively. The thick red histogram is the sum of the green and two blue lines. Panel (c) shows the level scheme for ^{34}Mg proposed in the present work.

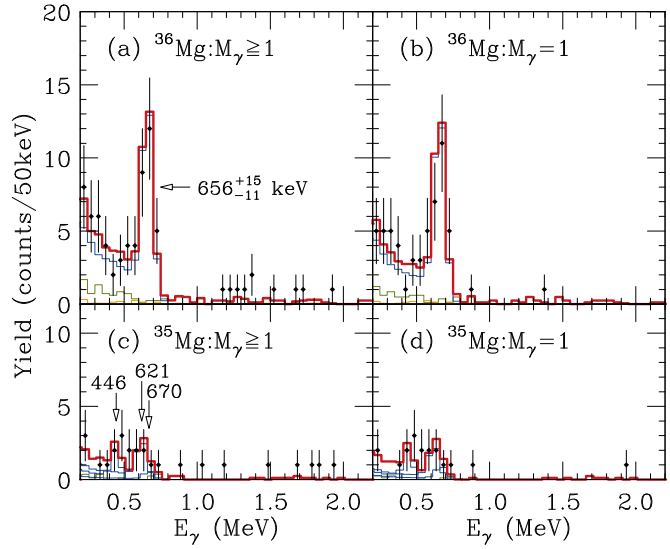

FIG. 8. (Color online) Gamma-ray energy spectra for the ^{1}H(^{36}Mg,^{36,35}Mgγ) reactions. Panels (a) and (b) are $M_\gamma \geqq 1$ and $M_\gamma = 1$ spectra, respectively, for the inelastic reaction channel. Panels (c) and (d) are the respective $M_\gamma \geqq 1$ and $M_\gamma = 1$ spectra for the neutron-removal channel from ^{36}Mg. The solid circles indicate the experimental data. The thin green and blue histograms show the background and simulated spectra of the $2^+_1 \rightarrow 0^+_1$ transition, respectively. The thin orange histograms in (a) and (b) indicate the contributions from the neutron-removal channel. The thick red histogram is the sum of the thin green, blue, and orange lines.

excitation cross sections for the 658-, 2011- and 3194-keV states were deduced to be 62(5) mb, 5(2) mb, and 10(2) mb, respectively. The cross section for population of the 2^+_1 state was also extracted from Fig. 6(b), and was measured to be 63(5) mb, which is consistent with the value quoted above.

The proton inelastic scattering cross section for the 2^+_1 state in ^{34}Mg was previously reported by Elekes *et al.* [46] to be 111(37) mb. However, in that study, they did not treat the feeding from higher-lying states because of insufficient statistics. Therefore, this value should correspond to the total transition strength of the $2^+_1 \rightarrow 0^+_1$ γ ray and is consistent with the value deduced in the present work of 78(6) mb.

5. ^{36}Mg

The γ-ray energy spectra for ^{36}Mg deduced in the present work are provided in Fig. 8. A single γ-ray transition at 656^{+15}_{-11} keV was identified, which is consistent with the first 2^+ state previously reported at 660(6) keV [47] and 662(6) keV [22]. The cross section for population of the 2^+ state and the total strength of the 656-keV transition were determined to be 47(8) mb and 49(8) mb, respectively.

De-excitation γ rays in ^{35}Mg were previously reported at 446(5), 621(7), and 670(8) keV [48]. We now discuss the influence of these γ rays in the ^{36}Mg spectra displayed in Figs. 8(a) and 8(b). Figures 8(c) and 8(d) are γ-ray energy spectra for ^{35}Mg obtained from the one-neutron removal channel from ^{36}Mg for $M_\gamma \geqq 1$ and $M_\gamma = 1$, respectively. Although the number of statistics in the one-neutron removal channel was relatively low, the spectra are consistent with the previous results [48].

Based on the estimated mass resolution for outgoing particles and the decomposition analysis using the ^{35}Mg spectra, γ rays from ^{35}Mg were estimated to modify the 656-keV γ-ray yield by approximately 2%. Note that the thin orange histograms in Figs. 8(a) and 8(b) indicate the contributions from the neutron-removal channel. It is important to realize that the γ rays in ^{35}Mg were taken into account when deducing the cross sections for the ^{36}Mg inelastic reaction channel discussed above.

In the present experiment, almost all of the 656-keV transition strength was attributed to the direct population of the 2^+_1 state, and no de-excitation γ rays from the higher-lying states were identified. However, in Ref. [22], a γ-ray cascade starting from a level at 2032 keV was reported. To discuss the contribution to the transition strength of the $2^+_1 \rightarrow 0^+_1$ transition from higher-lying states in the inelastic scattering spectra, we estimated the amount of feeding from the 2032-keV state. The contribution was calculated to be 2(5) mb, which is consistent with the difference between the cross sections for the population of the 2^+_1 state and the total transition strength of the 656-keV γ ray. Accordingly, the feeding proportion decreases along the magnesium isotopic chain from 40(13) % in ^{32}Mg, through 24(5) % in ^{34}Mg, to 4(11) % in ^{36}Mg. This trend agrees with the plausible assumption that the neutron separation energy of an isotope with a greater neutron excess is reducing.

B. Deformation lengths

Angle-integrated cross sections for the neutron-rich nuclei in the mass region were analyzed using coupled-channel calculations with the ECIS97 code [49] and the global potential WP09 [23], which was suggested to provide isospin-dependent optical potentials for analyzing proton and neutron scattering

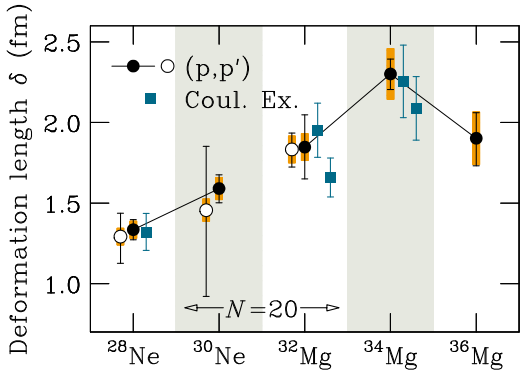

FIG. 9. (Color online) Deformation lengths of ^{28,30}Ne and ^{32,34,36}Mg. The solid circles indicate the present results while the open circles were estimated from the 2_1^+ cross sections reported in Refs. [26,29,38]. The square symbols are deformation lengths from Coulomb excitation experiments [10,44,45,50].

on nuclei far from stability, was employed for the incoming and outgoing channels. This parameter set is based on data from stable isotopes and light unstable nuclei. The use of the WP09 potential is suitable for the present analysis in terms of the beam energies, masses, and isospins of the nuclei. The inelastic transition potentials were based on the vibrational model for ^{28}Ne and the rotational model for the other nuclei, i.e., the ratio of $E_x(4_1^+)$ and $E_x(2_1^+)$ in each nucleus.

In proton inelastic studies, an optical-potential dependence of deformation parameters was discussed frequently in the past. To estimate the dependence, we compared the deformation lengths obtained from different optical potentials. For the proton inelastic scattering reactions we used the KD02 [24] and CH89 [25] global optical potentials, because they have been tested in numerous previous studies on unstable nuclei (see, for example, Ref. [29]). However, these potentials were based on data from stable nuclei and is not completely suitable to the present experimental condition. We compared the deformation lengths obtained from those potentials and the WP09 potential, and assigned the systematic error of each nuclei as the standard deviation among all the optical potentials.

The deformation lengths, $\delta_{(p,p')}$, are summarized in Table II and Fig. 9. In the figure, the solid and open circles indicate the deformation lengths deduced in the present work and those that have been estimated using the WP09 optical potential from the cross sections for the 2_1^+ states reported in Refs. [26,29,38], respectively. The thin black and thick orange error bars on the circles represent statistical and systematic errors, respectively. For each nucleus studied in the present work, systematic and statistical errors are typically similar in magnitude. Note that the deformation length of ^{28,30}Ne and ^{32}Mg agree with those deduced in previous studies in a satisfactory manner.

IV. DISCUSSION

A. Proton and neutron contributions to the quadrupole collectivity

To discuss the characteristic difference between the quadrupole collectivities associated with protons and neutrons, the current results can be compared to the collectivity estimated from reduced transition probabilities, B(E2), that were deduced from the Coulomb excitation of ^{28}Ne [50], ^{32}Mg [10,45], and ^{34}Mg [44,45]. In Fig. 9, square symbols represent the deformation lengths extracted from the $B(\mathrm{E2}\uparrow)$ values, where the relation, $\delta_C = 4\pi\sqrt{B(\mathrm{E2}\uparrow)}/3eZR$, was used and a charge radius parameter $R = 1.2A^{1/3}$ [51] was adopted. According to the systematic study by Bernstein, Brown, and Madsen [52], the ratio of the neutron and proton multipole matrix elements, M_n/M_p, is expressed as

$$\frac{M_n}{M_p} = \frac{b_p}{b_n}\left[\frac{\delta_{(p,p')}}{\delta_C}\left(1+\frac{b_n}{b_p}\frac{N}{Z}\right)-1\right],$$

which is a function of the deformation lengths obtained from the proton inelastic scattering $\delta_{(p,p')}$, and Coulomb excitation δ_C. The term b_n/b_p is the ratio of the sensitivity parameters for neutrons and protons, which is approximately equal to 3 for the proton inelastic scattering in the energy region of the present work [52]. When $\delta_{(p,p')}/\delta_C = 1$, $M_n/M_p = N/Z$, that is, it is independent of the sensitivity parameters.

As shown in Fig. 9, the deformation lengths of ^{28}Ne and ^{32,34}Mg deduced from proton inelastic scattering and Coulomb excitation are identical within experimental uncertainties, which indicates that the M_n/M_p ratios for the 2_1^+ states are similar to N/Z in those nuclei. Therefore, hindrance of neutron collectivity originating from a closed neutron shell is not significant in these systems.

TABLE II. Deformation lengths and parameters of ^{28,30}Ne and ^{32,34,36}Mg.

Nucleus	$\sigma(2_1^+)$ (mb)	$\delta_{(p,p')}$ (fm)	$\beta_{(p,p')}$
^{28}Ne	23(2)	1.33 ± 0.06 (stat) ± 0.05 (syst)	0.39 ± 0.02 (stat) ± 0.01 (syst)
	22(5) [38]	$1.29^{+0.15}_{-0.16}$ (stat) ± 0.05 (syst)[a]	$0.37^{+0.04}_{-0.05}$ (stat) ± 0.01 (syst)[a]
^{30}Ne	37(4)	$1.59^{+0.08}_{-0.09}$ (stat) ± 0.07 (syst)	$0.45^{+0.02}_{-0.03}$ (stat) ± 0.02 (syst)
	30(18) [26]	$1.46^{+0.40}_{-0.53}$ (stat) ± 0.06 (syst)[a]	$0.41^{+0.11}_{-0.15}$ (stat) ± 0.02 (syst)[a]
^{32}Mg	40^{+9}_{-8}	1.85 ± 0.20 (stat) ± 0.08 (syst)	$0.51^{+0.06}_{-0.05}$ (stat) ± 0.02 (syst)
	47.6(53) [29]	$1.83^{+0.10}_{-0.11}$ (stat) ± 0.09 (syst)[a]	0.50 ± 0.03 (stat) ± 0.02 (syst)[a]
^{34}Mg	63(5)	$2.30^{+0.09}_{-0.10}$ (stat) ± 0.16 (syst)	0.62 ± 0.03 (stat) ± 0.05 (syst)
^{36}Mg	47(8)	$1.90^{+0.16}_{-0.17}$ (stat) ± 0.16 (syst)	$0.50^{+0.04}_{-0.05}$ (stat) ± 0.04 (syst)

[a] $\beta_{(p,p')}$ and $\delta_{(p,p')}$ were deduced from the cross sections for 2_1^+ states reported in Refs. [26,29,38] using the WP09 optical potential [23].

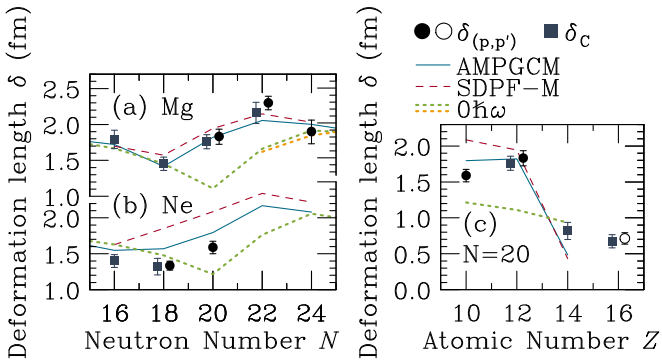

FIG. 10. (Color online) Systematics of deformation lengths around the island-of-inversion region. Panels (a), (b), and (c) are for Mg isotopes, Ne isotopes, and $N = 20$ isotones, respectively. The squares indicate the experimental results from the Coulomb excitation reactions [10,44,45,50,51,53–55]. Solid (open) circles are the deformation lengths estimated from proton inelastic scattering reactions in the present (previous [56]) work. The solid blue and dashed red lines are theoretical predictions of AMPGCM [57–59] and SDPF-M [11], respectively. The green and orange dotted lines represent $0\hbar\omega$ shell-model calculations [60,61].

B. Systematics of quadrupole deformation

The present results provide improved deformation lengths for ^{28,30}Ne, ^{34}Mg, and a new measurement for ^{36}Mg. Hence, systematic trends along Ne and Mg isotopic chains and the $N = 20$ line have now been extended. Figure 10 illustrates systematics of quadrupole deformation lengths. The squares indicate results determined from Coulomb excitation experiments [10,44,45,50,51,53–55], where the values for ^{32}Mg and ^{34}Mg were weighted averages of the results shown in Fig. 9. The solid and open circles represent the deformation lengths derived from proton inelastic scattering reactions in the present work and previous studies [56], respectively.

The deformation lengths of the Mg isotopes, which are displayed in Fig. 10(a), increase from $N = 18$ to 22. However, the deformation length of ^{36}Mg suggests that δ decreases beyond $N = 22$, at least ^{36}Mg ($N = 24$). It is noted that the deformation length deduced in the present work is consistent with the preliminary B(E2) measurement for ^{36}Mg [62]. Along the neon isotopic chain, presented in Fig. 10(b), the deformation length increases from $N = 18$ to 20, indicating that the collectivity of ^{30}Ne is significant despite the conventional magic number ($N = 20$). Thus, the present results support the loss of magicity in ^{30}Ne, that is suggested by the trend of 2_1^+ energies. As displayed in Fig. 10(c), the deformation lengths of the $N = 20$ isotones are observed to change somewhat suddenly between magnesium and silicon. Note that the deformation length of ^{30}Ne is much larger than those of ^{34}Si and ^{36}S, but is comparable to that of ^{32}Mg.

Figure 10 also displays several theoretical studies that can be compared to the experimental results; the solid blue and dashed red lines are predictions by AMPGCM [57–59] and the shell model with the SDPF-M effective interaction [11], and the green and orange dotted lines are shell-model calculations in the $0\hbar\omega$ model space reported by Caurier *et al.* [60] and Nowacki *et al.* [61], respectively. The theoretical deformation lengths were calculated from predicted B(E2) values in the same manner as discussed above. For ^{30}Ne and ^{36}Mg, the experimental electromagnetic deformation lengths (δ_C) are currently unknown. The δ_C values are assumed to be equal to the deformation lengths deduced from the proton inelastic scattering ($\delta_{(p,p')}$) because $\delta_C \approx \delta_{(p,p')}$ for neighboring nuclei and, therefore, the assumption is reasonable.

For magnesium isotopes, the AMPGCM and SDPF-M calculations, which implement configuration mixing around $N = 20$, predict that the deformation lengths increase from $N = 18$ to 22 and decrease gradually beyond $N = 22$, and, therefore, the predictions reproduce the deformation lengths obtained in the present experiment in a satisfactory manner. The calculation by Caurier, however, fails to reproduce the large collectivity at $N = 20$, but it reproduces the deformation length of ^{36}Mg somewhat well. In the neon isotopic chain, the AMPGCM and SDPF-M predictions reproduce the increase of deformation lengths at $N = 20$ although they both systematically overestimate the experimental results.

It is evident from Figs. 10(a) and 10(b) that the general pattern of the deformation lengths of neutron-rich Ne isotopes is similar to that of Mg. The ratios of deformation lengths of neon and magnesium isotones, δ_C(Ne)/δ_C(Mg), are provided in Fig. 11(a) as a function of neutron number, however, it should be noted that δ_C for ^{30}Ne was substituted by $\delta_{(p,p')}$. The ratios are approximately constant, at least up to $N = 20$, and the deformation lengths of the Ne isotopes are $\sim 10\%$ smaller than their Mg counterparts. Theoretical predictions

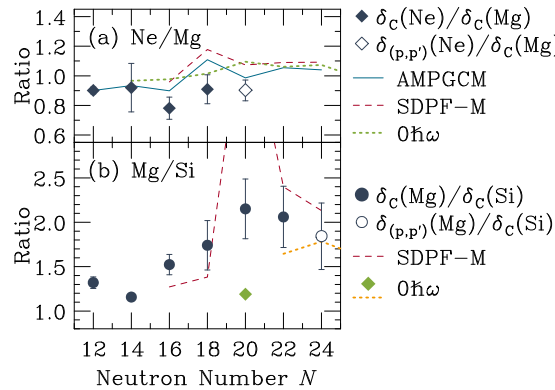

FIG. 11. (Color online) Ratio of deformation lengths of isotones around the island of inversion. Panels (a) and (b) show the ratios of Mg and Ne isotones and Si and Mg isotones, respectively. The solid diamonds (circles) were calculated from the deformation lengths obtained from Coulomb excitation of Ne and Mg (Mg and Si) isotones. The open diamond (circle) shows a ratio obtained from the Coulomb excitation of ^{32}Mg (^{38}Si) and the present result of ^{30}Ne (^{36}Mg). The dashed red and solid blue lines are the theoretical predictions by SDPF-M [11] and AMPGCM [57,58], respectively. The dotted green line in panel (a) and the green diamond in panel (b) are the $0\hbar\omega$ shell-model calculations from Ref. [60]. The dotted orange line in panel (b) represents the $0\hbar\omega$ shell-model calculations from Ref. [61].

of AMPGCM, the SDPF-M shell model and the shell model in a $0\hbar\omega$ model space, which are indicated by the solid blue, dashed red, and dotted green lines, respectively, are also presented in Fig. 11(a). In the cases of AMPGCM and SDPF-M, an increase of the ratio occurs at $N \geqq 18$, where both theories predict that $2\hbar\omega$ configurations dominate the ground state in Ne nuclei. The $0\hbar\omega$ shell model also predicts an increase at $N \geqq 20$. However, the experimental tendency does not appear to depend on whether the isotones lie inside (where $2\hbar\omega$ intruder configurations dominate) or outside of the island of inversion. This suggests that the structures of Ne and Mg isotones develop in a similar manner as the function of neutron number. When $\delta_{\rm C} = \delta_{(p,p')}$, which is probable for the mass region discussed here, the quadrupole matrix element per a nucleon (M_0) is defined as $M_0 = M_p/Z = M_n/N$. The ratio $\delta_{\rm C}({\rm Ne})/\delta_{\rm C}({\rm Mg})$ is essentially identical to the ratio of the matrix element per nucleon, that is, $M_0({\rm Ne})/M_0({\rm Mg}) \approx 0.9$. Therefore, quadrupole collectivity per nucleon for Ne isotopes can be considered to be uniformly suppressed compared to that of the corresponding magnesium isotone in the range $N = 12$–20.

To document the development of $2\hbar\omega$ configuration in Mg isotopes more thoroughly, Fig. 11(b) provides the ratio of deformation lengths of Mg and Si isotones, $\delta_{\rm C}({\rm Mg})/\delta_{\rm C}({\rm Si})$, at each neutron number, where $\delta_{\rm C}$ for ^{36}Mg was substituted by $\delta_{(p,p')}$. The experimental deformation lengths of the Si isotopes were adopted from Refs. [51,55]. The ratio gradually increases with neutron number, starting from isotopes at stability, and then begins to decrease beyond $N = 20$. It should be realized that the low-lying states in Si isotopes discussed here are described well by $0\hbar\omega$ configurations, and therefore, the enhancement of $\delta_{\rm C}({\rm Mg})/\delta_{\rm C}({\rm Si})$ highlights the development of intruder configurations in Mg isotopes relative to their Si isotonic counterparts.

Furthermore, Fig. 11(b) provides theoretical predictions by the shell model with the SDPF-M effective interaction [11] (dashed red line), and also in the $0\hbar\omega$ model space [60,61] (green diamond and dotted orange line). The SDPF-M shell model predicts an increase in the intruder configuration mixing from ^{30}Mg to ^{32}Mg, and then a decrease from ^{32}Mg to ^{36}Mg. The overall trend of SDPF-M expresses well the evolution of the intruder configuration mixing along the Mg isotopic chain.

The systematics of the experimental ratios is generally reproduced well by the SDPF-M shell model, with the exception of $N = 20$, while the $0\hbar\omega$ shell-model calculations underestimate the ratios at $N = 20$ and 22. The discrepancy in the SDPF-M shell model at $N = 20$ is likely to be caused by a poor description of ^{34}Si, where the 0^+_1 and 2^+_1 states are dominated by normal and intruder configurations, respectively [55,63].

Because SDPF-M also reproduces the the 2^+_1 energies of ^{34}Mg and ^{36}Mg in a satisfactory manner, the decrease in the experimental ratio of the deformation lengths can be considered to result as a reduction in the dominance of intruder configurations from ^{34}Mg to ^{36}Mg.

Concerning configuration mixing in ^{36}Mg, the SDPF-M shell model predicts that intruder (normal) configurations are present at 60% (40%) in the ground state. This is consistent with the previous study [47] that stated ^{36}Mg contains a $0\hbar\omega$ component at a level of approximately 40%. The ratio for ^{36}Mg reported in the present work is consistent with the SDPF-M shell model. Because the ratio deduced in the present work is likely to be located between the predictions of SDPF-M and the $0\hbar\omega$ shell model, the result may indicate that ^{36}Mg is located in a competitive region between normal and intruder configuration.

V. SUMMARY

We have studied quadrupole collectivity in neutron-rich, even-even neon, and magnesium nuclei around $N = 20$ via proton inelastic scattering at approximately 50 MeV/nucleon. The experiment was performed using a liquid hydrogen target (CRYPTA), the TOMBEE spectrometer, and the DALI2 array at the RIPS beam line in RIKEN. By measuring de-excitation γ rays in coincidence with reaction products cross sections for population of the first 2^+ states were deduced. Deformation lengths were extracted from the angle-integrated cross sections, which were analyzed using the distorted-wave calculations. The deformation length of ^{36}Mg was determined for the first time, while those of ^{30}Ne and ^{34}Mg were determined with improved accuracy.

The experimental ratios of the deformation lengths of neon to magnesium isotones were found to be somewhat uniform ($\sim$0.9), which indicates that the evolution of the neutron shell structure is quite similar for these isotones. The trend of collectivity along the $N = 20$ isotonic chain further highlight the large deformation of ^{30}Ne, a nucleus that lies in the island of inversion.

Regarding the systematics of the ratios of the deformation lengths of magnesium to silicon isotones, the experimental data indicate a decrease in the role played by intruder configurations from ^{32}Mg to ^{36}Mg. This tendency is consistent with the SDPF-M shell-model calculation, which can reproduce 2^+_1 excitation energies and deformation lengths in magnesium isotopes in a satisfactory manner. In ^{36}Mg, the normal and intruder configurations are thought to compete against one another and this nucleus may, therefore, represent the neutron-rich edge of island of inversion in the magnesium isotopic chain.

To map the low-Z boundary of the island of inversion, collectivity should be investigated in neon isotopes that lie further from stability, namely, ^{32}Ne and ^{34}Ne. It is also noted that the structures of fluorine and oxygen isotopes beyond $N = 20$ are also important for investigating the boundaries of the island of inversion, despite the fact that these systems are unbound. New-generation RI-beam facilities such as RIBF, FRIB, SPIRAL2, RISP, and FAIR will offer a wealth of opportunities for such studies, and therefore, a more thorough understanding of the mechanisms responsible for the occurrence of the island of inversion should be possible in the near future.

ACKNOWLEDGMENTS

We would like to thank the RIKEN Ring Cyclotron staff members for their operation during the experiment. We are grateful to Professor S. Shimoura for fruitful discussions.

This research was partly realized in the framework of TÁMOP 4.2.4. A/2-11-1-2012-0001 "National Excellence Program–Elaborating and operating an inland student and researcher personal support system." The project was subsidized by European Union and co-financed by European Social Fund.

[1] O. Sorlin and M.-G. Porquet, Prog. Part. Nucl. Phys. **61**, 602 (2008), and references therein.
[2] A. Navin *et al.*, Phys. Rev. Lett. **85**, 266 (2000).
[3] H. Iwasaki *et al.*, Phys. Lett. B. **481**, 7 (2000).
[4] H. Iwasaki *et al.*, Phys. Lett. B. **491**, 8 (2000).
[5] S. Shimoura *et al.*, Phys. Lett. B **560**, 31 (2003).
[6] C. Thibault *et al.*, Phys. Rev. C **12**, 644 (1975).
[7] X. Campi *et al.*, Nucl. Phys. A **251**, 193 (1975).
[8] C. Détraz *et al.*, Phys. Rev. C **19**, 164 (1979).
[9] E. K. Warburton, J. A. Becker, and B. A. Brown, Phys. Rev. C **41**, 1147 (1990).
[10] T. Motobayashi *et al.*, Phys. Lett. B **346**, 9 (1995).
[11] Y. Utsuno *et al.*, Rhys. Rev. C **60**, 054315 (1999).
[12] B. Bastin *et al.*, Phys. Rev. Lett. **99**, 022503 (2007).
[13] S. Takeuchi *et al.*, Phys. Rev. Lett. **109**, 182501 (2012).
[14] A. Ozawa, T. Kobayashi, T. Suzuki, K. Yoshida, and I. Tanihata, Phys. Rev. Lett. **84**, 5493 (2000).
[15] A. Huck *et al.*, Phys. Rev. C **31**, 2226 (1985).
[16] A. Gade *et al.*, Phys. Rev. C **74**, 021302(R) (2006).
[17] F. Wienholtz *et al.*, Nature (London) **498**, 346 (2013).
[18] D. Steppenbeck *et al.*, Nature (London) **502**, 207 (2013).
[19] W. T. Pinkston and G. R. Satchler, Nucl. Phys. **27**, 270 (1961).
[20] P. H. Stelson and L. Grodzins, Nucl. Data Sheets. Section A **1**, 21 (1965).
[21] P. Doornenbal *et al.*, Phys. Rev. Lett. **103**, 032501 (2009).
[22] P. Doornenbal *et al.*, Phys. Rev. Lett. **111**, 212502 (2013).
[23] S. P. Weppner, R. B. Penney, G. W. Diffendale, and G. Vittorini, Phys. Rev. C **80**, 034608 (2009).
[24] A. J. Korning and J. P. Delaroche, Nucl. Phys. **A713**, 231 (2003).
[25] R. L. Varner *et al.*, Phys. Rep. **201**, 57 (1991).
[26] Y. Yanagisawa *et al.*, Phys. Lett. B **566**, 84 (2003).
[27] N. Aoi *et al.*, Phys. Lett. B **692**, 302 (2010).
[28] N. Aoi *et al.*, Phys. Rev. Lett. **102**, 012502 (2009).
[29] S. Takeuchi *et al.*, Phys. Rev. C **79**, 054319 (2009).
[30] H. Sakurai *et al.*, Eur. Phys. J. A **25**, s01 403 (2005).
[31] T. Kubo *et al.*, Nucl. Instrum. Methods Phys. Res. Sect. B **70**, 309 (1992).
[32] H. Ryuto *et al.*, Nucl. Instrum. Methods Phys. Res. Sect. A **555**, 1 (2005).
[33] S. Takeuchi *et al.*, RIKEN Accel. Prog. Rep. **36**, 148 (2003); arXiv:1403.5349.
[34] N. Aoi *et al.*, RIKEN Accel. Prog. Rep. **38**, 176 (2005).
[35] T. Kusaka *et al.*, IEEE Trans. Appl. Supercond. **14**, 310 (2004).
[36] H. Kumagai *et al.*, Nucl. Instrum. Methods Phys. Res. Sect. A **470**, 562 (2001).
[37] GEANT3, CERN Program Library Long Writeup W5013 (1993).
[38] Zs. Dombrádi *et al.*, Phys. Rev. Lett. **96**, 182501 (2006).
[39] ENSDF, NNDC Online Data Service, ENSDF database [http://www.nndc.bnl.gov/nndc/ensdf/].
[40] P. Fallon *et al.*, J. Phys.: Conf. Ser. **49**, 165 (2006).
[41] S. Michimasa *et al.*, Phys. Lett. B **638**, 146 (2006).
[42] P. Fallon *et al.*, Phys. Rev. C **81**, 041302(R) (2010).
[43] K. Yoneda *et al.*, Phys. Lett. B **499**, 233 (2001).
[44] H. Iwasaki *et al.*, Phys. Lett. B **522**, 227 (2001).
[45] J. A. Church *et al.*, Phys. Rev. C **72**, 054320 (2005).
[46] Z. Elekes *et al.*, Phys. Rev. C **73**, 044314 (2006).
[47] A. Gade *et al.*, Phys. Rev. Lett. **99**, 072502 (2007).
[48] A. Gade *et al.*, Phys. Rev. C **83**, 044305 (2011).
[49] J. Raynal, Coupled channel code ECIS97, also Notes on ECIS94 (unpublished).
[50] H. Iwasaki *et al.*, Phys. Lett. B **620**, 118 (2005).
[51] S. Raman, C. W. Nestor Jr., and P. Tikkanen, Atomic Data Nucl. Data Tables **78**, 1 (2001).
[52] A. M. Bernstein, V. R. Brown, and V. A. Madsen, Rhys. Lett. B **103**, 255 (1981).
[53] O. Niedermaier *et al.*, Phys. Rev. Lett. **94**, 172501 (2005).
[54] J. Gibelin *et al.*, Phys. Rev. C **75**, 057306 (2007).
[55] R. W. Ibbotson *et al.*, Phys. Rev. Lett. **80**, 2081 (1998).
[56] A. Hogenbirk *et al.*, Nucl. Phys. A **516**, 205 (1990).
[57] R. R. Rodríguez-Guzmán, J. L. Egido, and L. M. Robledo, Nucl. Phys. A **709**, 201 (2002).
[58] R. R. Rodríguez-Guzmán, J. L. Egido, and L. M. Robledo, Eur. Phys. J. A **17**, 37 (2003).
[59] R. R. Rodríguez-Guzmán, J. L. Egido, and L. M. Robledo, Phys. Lett. B **474**, 15 (2000).
[60] E. Caurier, F. Nowacki, A. Poves, and J. Retamosa, Phys. Rev. C **58**, 2033 (1998).
[61] F. Nowacki and A. Poves, Phys. Rev. C **79**, 014310 (2009).
[62] E. Caurier *et al.*, arXiv:1309.6955.
[63] F. Rotaru *et al.*, Phys. Rev. Lett **109**, 092503 (2012).